Purdue University

Purdue e-Pubs

PRISM: NNSA Center for Prediction of Reliability, Integrity and Survivability of Microsystems

Birck Nanotechnology Center

6-3-2010

Strain rate sensitivity of nanocrystalline Au films at room temperature

K Jonnalagadda

N Karanjgaokar

Joo lien Chee
Purdue University - Main Campus, joolien@purdue.edu

Dimitrios Peroulis
Birck Nanotechnology Center and School of Electrical and Computer Engineering, Purdue University, dperouli@purdue.edu

Follow this and additional works at: http://docs.lib.purdue.edu/prism

Part of the Nanoscience and Nanotechnology Commons

ELSEVIER

Strain rate sensitivity of nanocrystalline Au films at room temperature

K. Jonnalagadda [a], N. Karanjgaokar [b], I. Chasiotis [c,*], J. Chee [d], D. Peroulis [d]

[a] *Mechanical Engineering, Indian Institute of Technology Bombay, Mumbai 400 0076, India*
[b] *Mechanical Science and Engineering, University of Illinois at Urbana Champaign, Urbana, IL, USA*
[c] *Aerospace Engineering, University of Illinois at Urbana Champaign, Urbana, IL, USA*
[d] *Electrical Engineering, Purdue University, West Lafayette, IN, USA*

Abstract

The effect of strain rate on the inelastic properties of nanocrystalline Au films was quantified with 0.85 and 1.76 μm free-standing microscale tension specimens tested over eight decades of strain rate, between 6×10^{-6} and 20 s^{-1}. The elastic modulus was independent of the strain rate, 66 ± 4.5 GPa, but the inelastic mechanical response was clearly rate sensitive. The yield strength and the ultimate tensile strength increased with the strain rate in the ranges 575–895 MPa and 675–940 MPa, respectively, with the yield strength reaching the tensile strength at strain rates faster than 10^{-1} s^{-1}. The activation volumes for the two film thicknesses were 4.5 and 8.1 b^3, at strain rates smaller than 10^{-4} s^{-1} and 12.5 and 14.6 b^3 at strain rates higher than 10^{-4} s^{-1}, while the strain rate sensitivity factor and the ultimate tensile strain increased below 10^{-4} s^{-1}. The latter trends indicated that the strain rate regime 10^{-5}–10^{-4} s^{-1} is pivotal in the mechanical response of the particular nanocrystalline Au films. The increased rate sensitivity and the reduced activation volume at slow strain rates were attributed to grain boundary processes that also led to prolonged (5–6 h) and significant primary creep with initial strain rate of the order of 10^{-7} s^{-1}.

© 2010 Acta Materialia Inc. Published by Elsevier Ltd. All rights reserved.

Keywords: Nanocrystalline materials; Thin films; Ductility; Microvoids; Creep tests

1. Introduction

The high yield strength of nanocrystalline metals [1] has led to new possibilities for mechanically improved structural materials. However, the beneficial effect of nanocrystallinity is weighed by the increased strain rate sensitivity [2–7] and increased creep rates compared to films with larger grain size. Nanocrystalline metals allow for large material volumes occupied by grain boundaries that control dislocation nucleation [4,8] and grain boundary mediated creep [9] while affecting the relative contribution of thermal and stress driven inelastic processes [10–12]. These often competing mechanisms result in increased rate sensitivity which is not uniform across time scales: diffusion controlled processes are important at slow loading rates and may dominate in materials with large percentage of grain boundaries. This competition between grain boundary and intragranular deformation mechanisms is expected to control rate sensitivity and the activation volumes in nanocrystalline metals.

To date, experiments have been limited to a small range of strain rates, typically 10^{-6}–10^{-3} s^{-1} [3,7,13,14], which, although very indicative of the existence of rate sensitivity, investigated a narrow range of strain rates and did not clearly distinguish the effects of room temperature creep [15] and anelastic stress relaxation [16], which are present at slow strain rates, on the overall deformation. Steady-state creep rates for nanocrystalline face-centered cubic (fcc) metals at room temperature have been reported to be of the order of 10^{-10}–10^{-7} s^{-1} [17,18]. However, these rates are quite lower than the primary creep rate which is

---

* Corresponding author. Address: Aerospace Engineering, University of Illinois at Urbana Champaign, Urbana, IL 61801, USA. Tel.: +1 217 244 1474.

E-mail address: chasioti@illinois.edu (I. Chasiotis).

a function of the applied stress amplitude and affects the measurement of inelastic properties such as the elastic limit and the yield strength. Given that the stress within the high elastic limit of nanocrystalline metals can reach quite large values, it is evident that the primary creep rates in nanocrystalline metals subjected to high elastic stresses can be orders of magnitude higher than those reported in literature for bulk metals. Therefore, unless experiments span regimes of strain rate significantly broader than 10^{-6}–10^{-3} s^{-1}, it may not be possible to separate the effects of stress induced plasticity and creep. There are additional considerations that need to be accounted for: the mechanical response of metallic films has been shown to vary with film thickness [3,7,19]. Espinosa et al. [19] reported on an inverse thickness effect on the yield strength of Au and Al films. More recently, Chauhan and Bastawros [20] investigated in detail the interplay between grain size and film thickness.

This experimental investigation focuses on relationships between the stain rate and the inelastic mechanical properties of Au films with nanoscale grain size and micrometer thicknesses. For the first time, the strain rate regime of 10^{-6}–20 s^{-1} is spanned by microscale tension experiments in order to quantify the effect of competing deformation mechanisms with different intrinsic time scales on the mechanical response of thin films. To eliminate any film thickness effects, the specimen thickness was 20–40 times larger than the grain size. The measurements are corroborated by activation volume calculations, creep experiments to determine the primary and steady-state creep rates for nanocrystalline Au, and by fractographic studies to characterize the differences in damage evolution at slow and fast strain rates.

2. Experimental methods

2.1. Specimen preparation and materials characterization

The process of specimen fabrication included a 500 nm thick layer of thermal oxide that was grown on a silicon (1 0 0) wafer followed by a 2 μm thick photoresist layer, as seen in step (A) in Fig. 1a. After patterning the photoresist layer (step (B)), a trench was created in the oxide layer for depositing Au, as shown in step (C) in Fig. 1a. The photoresist layer was then removed and a 20 nm thick Ti layer was deposited to assist the adhesion of Au to oxide, which was deposited by RF sputtering. A second layer of 2 μm thick photoresist was then spin-coated and patterned to etch Ti/Au in a pattern that matched the final specimen dimensions, as shown in step (D) in Fig. 1a. Finally, the second photoresist layer was removed and the silicon underneath the Au layer was etched with XeF$_2$. The free-standing Au films were prepared as shown in schematic (E) in Fig. 1a after 30 cycles of etching, each lasting for 15 s. This process produced Au specimens with thicknesses of 1.76 and 0.85 μm and gauge width and length of 100 and 1000 μm, respectively, as shown in Fig. 1b.

Transmission electron microscopy (TEM), scanning electron microscopy (SEM) and X-ray diffraction (XRD) studies were conducted to determine the specimen thickness, average grain size and the texture of the Au films. Both in-plane and cross-sectional TEM samples were prepared to measure the grain size on the plane of the film and through the cross-section. For plan view TEM images, the 1.76 μm thick sample was mounted on a TEM grid to be ion milled for 30 min to obtain an electron transparent region. The bright field TEM micrograph in Fig. 2a was used to obtain the grain size distribution shown in Fig. 2b. The average grain size calculated from several TEM micrographs using the line average method was 30 ± 6 nm. From the diffraction pattern analysis it was found that the texture was predominantly (1 1 1) in the grain growth direction, with some evidence of (1 1 0). The wedge polishing technique was applied to obtain an electron transparent region for cross-sectional TEM sample preparation. In Fig. 2c, one can observe that the cross-section of the Au films is composed of several layers of deposition. Many grains were seen across the thickness of the film and the grain size was smaller in the cross-section compared to its in-plane dimensions. Finally, the cross-sectional SEM image in Fig. 2d shows the coherent cross-section of the Au films.

Table 1 provides the details of the grain size, texture and lattice constant for each film thickness, as obtained by XRD. The correctly determined value of the Au lattice constant ensures the accuracy of the XRD measurements. Furthermore, the film texture is similar to previous reports for sputtered Au thin films [7]. For all practical purposes the grain size of the two film thicknesses is considered the same ($\sim$ 40 nm) in discussing the experimental results.

2.2. Microscale tension experiments

Conducting experiments at time scales varying from microseconds to hours requires a force sensor with fast time response, long-term stability and rate-independent compliance, as well as displacement actuators with fast response and minimal inertia. Similarly, strain must be measured directly from the specimen gauge section, preferably using a fine speckle pattern generated on the free-standing specimens with submicron scale particles. Using a custom-built apparatus, silicon particles with 1 μm average size and a homogeneous distribution were dispersed as shown in Fig. 3 and according to the method described in Ref. [21]. The particles adhered to the free-standing thin film specimens due to van der Waals forces, providing high-fidelity full-field displacements via digital image correlation (DIC) [21] so that both axial and transverse displacements could be calculated. This method provided ~25 nm resolution in film extensions [21], which is comparable to the resolution by experiments conducted inside scanning or transmission electron microscopes, with the additional capability to probe strain rates varying by almost eight orders of magnitude, which is not possible in experiments conducted inside analytical chambers.
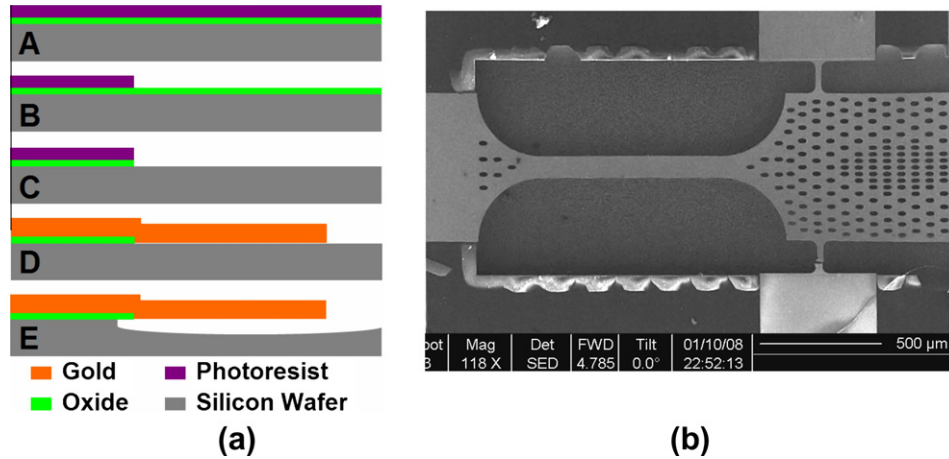
Fig. 1. (a) Fabrication steps for microscale Au specimens: (A) deposition of thermal oxide and spin-coating of photoresist for patterning; (B) patterning of the photoresist by photolithography; (C) etching the oxide layer; (D) removal of photoresist and sputter deposition of Au layer; and (E) dry etching of silicon under the specimens. (b) SEM micrograph of a free-standing test specimen.
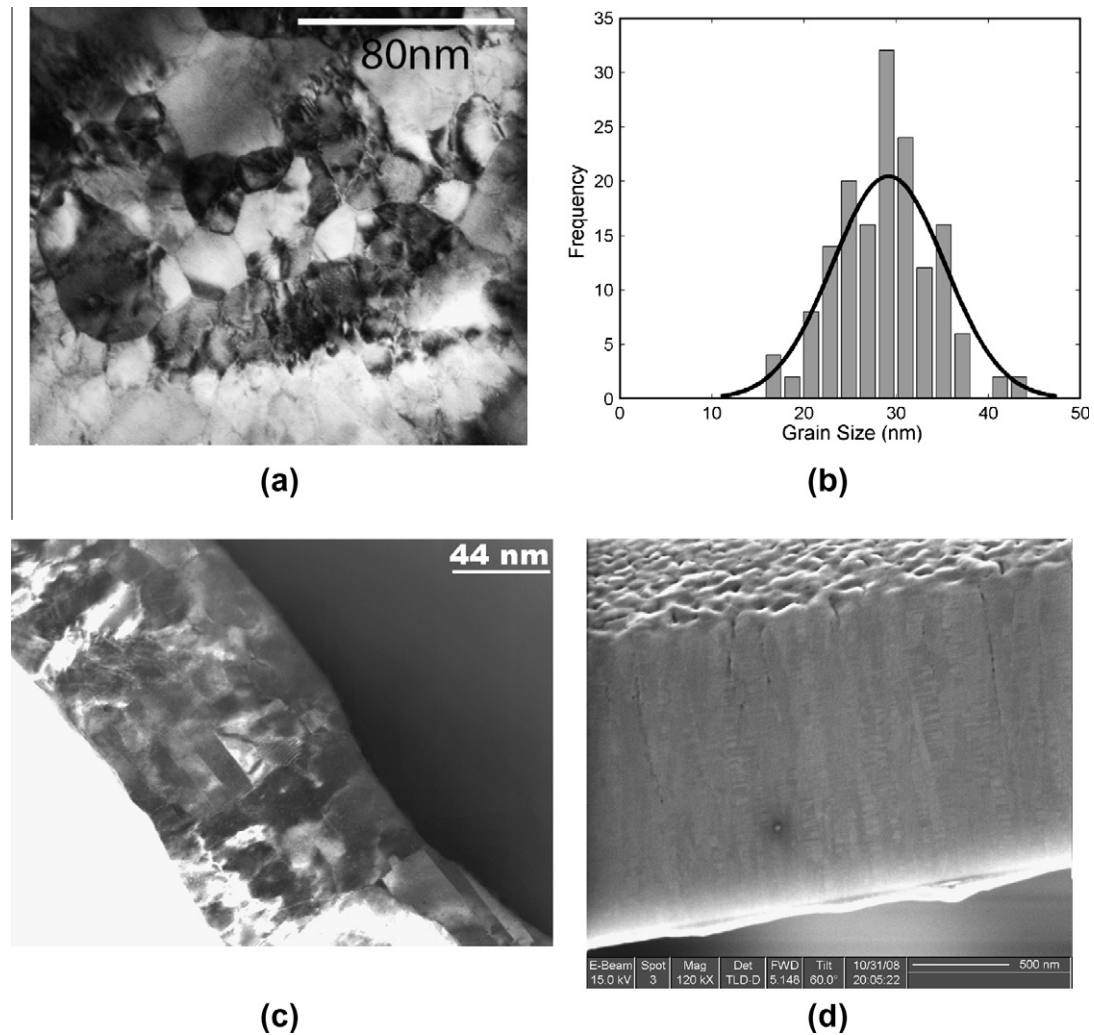

Fig. 2. (a) Planar view TEM micrograph of an Au thin film; (b) distribution of grain sizes; (c) cross-sectional TEM image; and (d) SEM image of the cross-section showing the grain structure through the film thickness. The scale bar in (c) is set to 44 nm, which is the grain size as measured by XRD.

In order to span the rate regime of 10^{-6}–$20\ \mathrm{s}^{-1}$, two loadcell types were employed. At loading rates of up to $10^{-3}\ \mathrm{s}^{-1}$ a strain gauge loadcell was used, whereas for strain rates 10^{-3}–$20\ \mathrm{s}^{-1}$, a piezoresistive loadcell was

Table 1
X-ray diffraction results for the two Au film thicknesses.

Film thickness (µm)	Grain size (nm)	Texture	Lattice constant (nm)
0.85	44	{1 1 1}	0.4091
1.76	38	{1 1 1}	0.4095

Fig. 4. Stress vs. strain curves of two free-standing Au film specimens tested at the same strain rate of 6×10^{-3} s^{-1} using a strain gauge and a piezoresistive loadcell.

employed. A modular microscale tensile testing apparatus was built to accommodate the two transducers. A digital camera with maximum frame rate of 15 fps was used at low strain rates (10^{-6}–10^{-3} s^{-1}) and a high speed camera with 100,000 fps was used for the higher strain rate experiments (10^{-3}–20 s^{-1}).

The strain in each experiment was computed from the optical images, so the use of two apparatuses with components of different compliance did not affect the calculation of full-field displacements or strains by DIC. In order to compare the measurements of the two apparatus configurations, Au specimens of 1.76 µm thickness were tested at the same strain rate (6×10^{-3} s^{-1}) by using the strain gauge loadcell (slow) and the piezoresistive loadcell (fast) configuration, and the two stress vs. strain curves are shown in Fig. 4. The two curves overlap almost until failure, which emphasizes the accuracy and repeatability of the present experiments.

3. Results and discussion

Earlier works by Emery and Povirk [13,14], Chasiotis et al. [3] and Wang and Prorok [7] presented strain rate data for Au films that spanned strain rates between 10^{-6} and 10^{-3} s^{-1}. We extended this range to about eight decades of strain rate, between 6×10^{-6} and 20 s^{-1}, spanning time scales prone to different inelastic deformation mechanisms, such as creep and dislocation plasticity.

3.1. Rate-dependent mechanical behavior of Au films

Fig. 5a and 5b show the engineering stress vs. strain curves at strain rates of 6×10^{-6}–20 s^{-1}. The precise strain
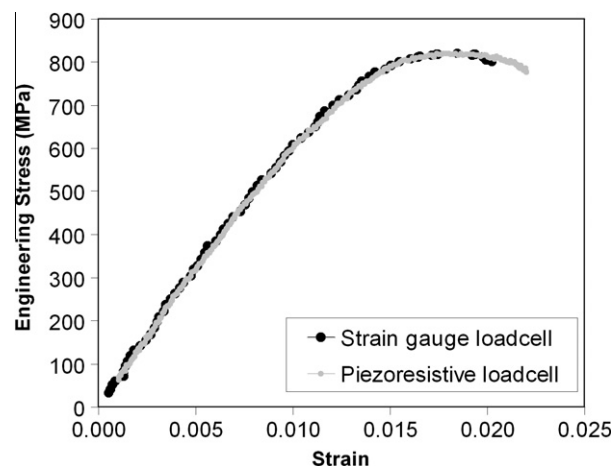
rate was determined directly from the strain measured by the CCD camera. The engineering stress vs. strain plots have a clear linearly elastic region up to large stresses, followed by yield and limited strain hardening before final failure. Unlike previous literature reports, clear shear localization occurred at all rates but the width of the shear band decreased with increasing applied strain rate, as was evidenced by the measured ultimate strain. The initial slopes of all stress vs. strain curves were very close to each other, resulting in average elastic moduli of 64.7 ± 6.5 and 66.6 ± 2.5 GPa for 0.85 and 1.76 µm thick specimens, respectively (averaging 66 ± 4.5 GPa for both thicknesses). These values are smaller than the modulus of bulk Au, reported as 78 GPa [22,23], but very consistent with modulus values reported for most tensile experiments with Au films in the literature [3,7,13,14,19,24,25]. Different authors have attributed the smaller elastic modulus to microstructure [14] and grain boundary relaxation [24], and, in the case of significantly smaller stiffness values, to film porosity [3,26]. Film porosity has been reported to be the reason for low elastic modulus, yield strength and tensile strength
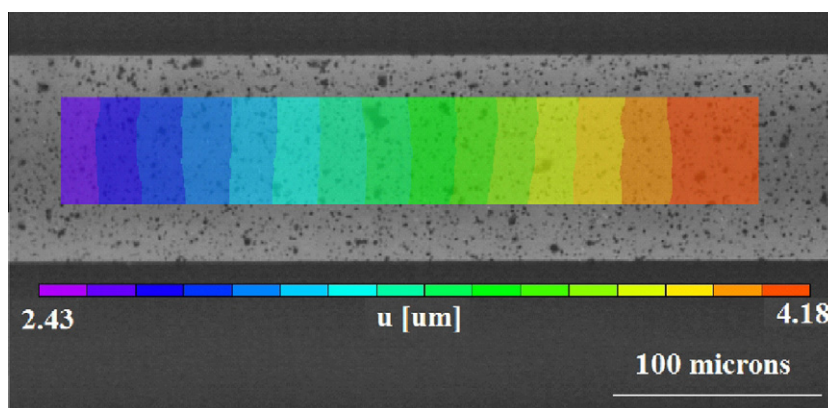

Fig. 3. Speckle pattern on the gauge section of a microscale sample with superposed resolved displacement field. The 2.43 µm offset in the displacement field originates in the rigid body translation of the left grip of the specimen, which is attached to a compliant loadcell. The excellent specimen alignment is evidenced by the alignment of the displacement contours.
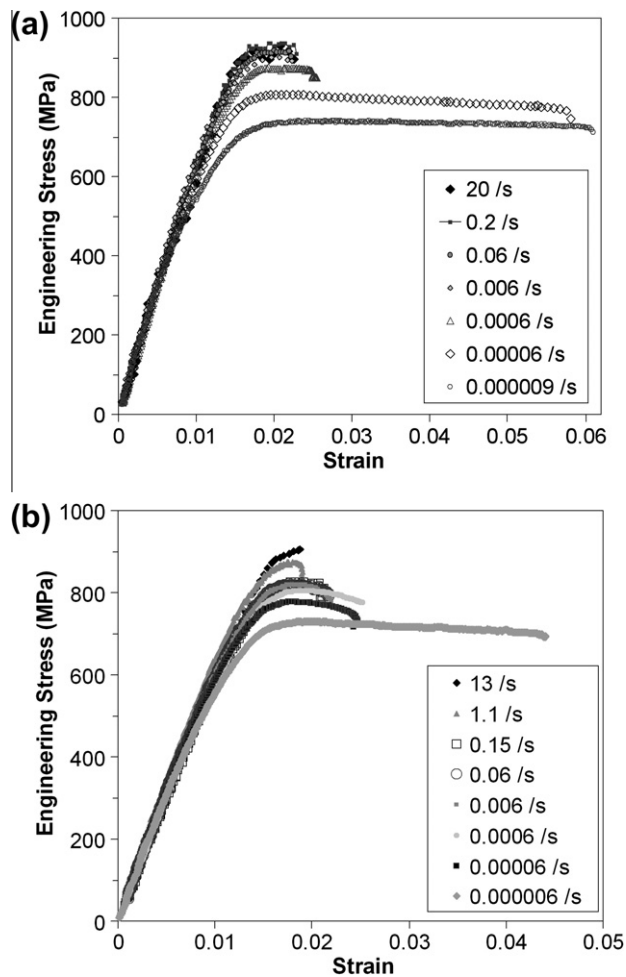
Fig. 5. Stress–strain curves at different strain rates for (a) 0.85 μm and (b) 1.76 μm thick Au films.

[3,27]. Hugo et al. [27] reported that DC magnetron-sputtered (DCMS) Cu films had a lower elastic modulus compared to pulsed laser-deposited films. Based on TEM images, the authors concluded that the reduced stiffness was a result of porosity in DCMS films due to gas entrapment. Similarly, Chasiotis et al. [3] explained the low modulus and yield strength of electrodeposited and evaporated Au films tested at several strain rates by means of film porosity. As shown in Fig. 2a, c and d, there were no signs of porosity in the present Au films, which is also corroborated by the high values of 0.2% yield and ultimate tensile strengths.

On the other hand, nanocrystallinity favors the larger contribution of grain boundary compliance to the overall film stiffness. Therefore, the reduced elastic modulus may be associated with the increased grain boundary volume that is occupied by disordered Au atoms contributing to the increased film compliance [28,29]. This argument, however, does not provide a general mechanism for nanocrystalline materials. Experiments conducted by Jonnalagadda et al. [21] on 400 nm thick nanocrystalline Pt films with an average grain size of 25 nm resulted in an elastic

modulus that was independent of the strain rate and nearly the same as that of bulk Pt.

Some literature reports have discussed the reduced elastic modulus in terms of irreversible grain boundary and intra-grain dislocation processes, which are eliminated after an initial process of material loading/unloading [30]. The elastic modulus reported in this work was consistent at all time scales, and therefore initial loading relaxations owed to grain boundary diffusional processes can be ruled out. Furthermore, the loading and unloading moduli measured in the present experiments were identical at slow and very fast loading rates, which rules out the presence of such initial irreversible deformation processes [30]. On the other hand, it has been reported that relaxation processes associated with grain boundary sliding and mediated by dislocation pinning may be partially reversible and result in anelastic behavior and rate-sensitive moduli, as reported for micron-sized grains [31,32]. The rate-insensitive modulus reported in this work indicates that, if present, the rate of such anelastic deformation processes may be negligible at the time scales of our measurements and for the particular Au films. Similar rate insensitivity was reported by Jonnalagadda et al. [21], which implies that the specific material fabrication and post-processing treatments may determine the anelastic behavior of metallic films.

The inelastic properties of the Au films, i.e. the elastic limit, the yield strength and the ultimate tensile strength, as shown in Fig. 6a and b, were significantly higher than the literature values at comparable strain rates [3,7,19,13,14] due to the Hall–Petch effect, which was pronounced for the particular films with ~40 nm grain size [1,2,6]. Furthermore, the trends in the elastic limit, the yield strength and the ultimate tensile strength in the range of almost eight decades of strain rate in Fig. 6a and b point to strain rate sensitivity, which is in agreement with the previous results for Au [3–7,19] and other nanocrystalline fcc materials, such as Cu [15] and Ni [15]. In particular, the elastic limit increased by 86% and 126% from the slowest (10^{-6} s^{-1}) to the fastest (20 s^{-1}) loading rate for 0.85 and 1.76 μm thick specimens, respectively, whereas the 0.2% yield strength increased by 47% and 38%, respectively. The ultimate tensile strength was more consistent and varied by only about 25% for both film thicknesses. It is noteworthy that at rates equal or larger than 10^{-1} s^{-1} the yield strength and the ultimate tensile strength of the 0.85 μm thick films virtually coincided at about 900 MPa, pointing to an upper limit in the tensile yield and ultimate strength for the particular nanocrystalline Au films.

The plot of the ultimate strain vs. strain rate in Fig. 7 can serve to further understand the mechanisms at work after yielding: the ultimate strain was very consistent at strain rates of 10^{-4}–20 s^{-1}, but a major increase took place at <10^{-4} s^{-1}, with the ultimate strain reaching 6–7%. This large strain was accommodated by a wide localization band at the site of shear failure that was between 45° and 54° with respect to the applied load. Strain localization occurred at high engineering stresses (>600 MPa) and
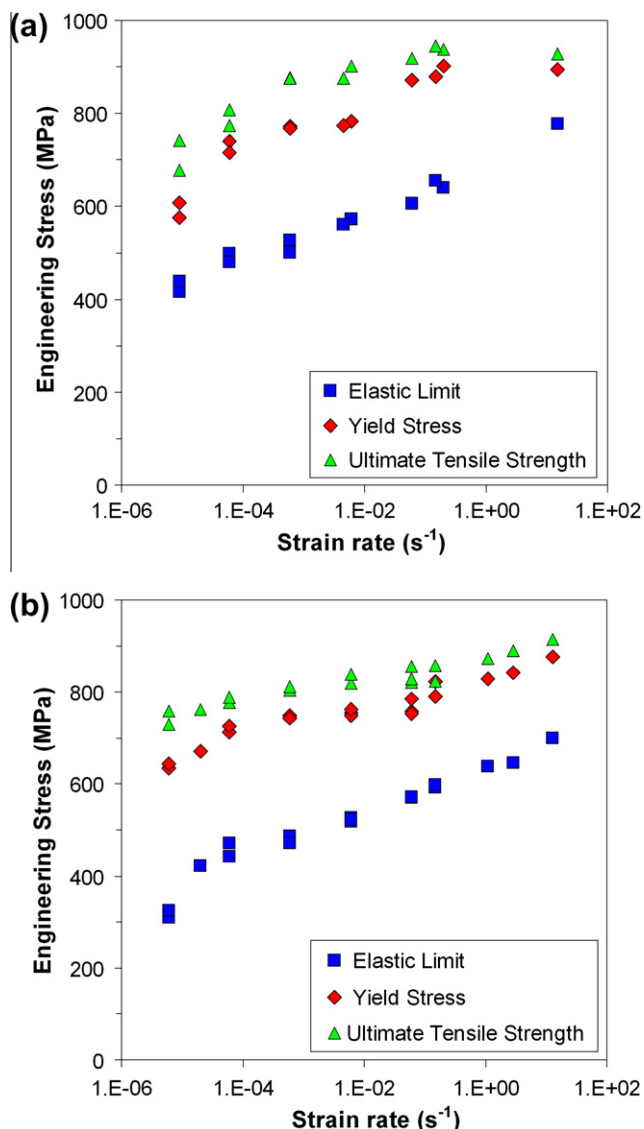
Fig. 6. Elastic limit, yield strength and ultimate tensile strength as a function of strain rate for (a) 0.85 μm and (b) 1.76 μm films.

Fig. 7. Failure strain vs. strain rate for 1.76 and 0.85 μm thick Au specimens.

curves (8 h loaded, 3 h unloaded Au films) is shown in Fig. 8, indicating the prolonged primary creep in the first creep cycle, which spanned 5–6 h. The primary creep rate and its duration both increased, with the magnitude of stress being of the order of $10^{-7}\,s^{-1}$ at $t = 0^{+}$ under an applied stress of 250 MPa. The increased creep rates are due to the contribution of diffusional processes at the extended grain boundaries in nanocrystalline Au. Therefore, even larger primary creep rates are expected to take place at higher, nominally elastic, stresses. Given this long duration of primary creep, it is concluded that the slow strain rate experiments (10^{-6}–$10^{-5}\,s^{-1}$) are strongly influenced by room temperature primary creep. On the other hand, at the faster strain rates (10^{-4}–$20\,s^{-1}$), inelastic processes are driven by intragranular dislocation processes, although dislocation nucleation still occurs at grain boundary ledges and triple junctions [8].

As will be shown later, the mechanical behavior of Au films at $\leqslant 10^{-5}\,s^{-1}$ showed increased rate sensitivity and a

was accompanied, as will be shown later, by significant void formation and growth inside a shear band. At the same strain rate ($10^{-4}\,s^{-1}$), the elastic limit and the yield strength plots changed slopes compared to the faster rates of 10^{-4}–$20\,s^{-1}$.

These changes in slope and the increased ductility at slow loading rates stemmed from the competition between the deformation due to the externally applied stress and the room temperature creep/stress relaxation processes that can have high rates for thin films [3]. To further elucidate this point, the room temperature primary and the steady-state creep rates were quantified by creep experiments with 1.76 μm thick Au films and at applied stresses smaller than the elastic limit recorded at the slowest strain rate ($6 \times 10^{-6}\,s^{-1}$): The films were held at constant stress for up to 21 h, then unloaded for 3 h, and this loading profile was repeated three times. The creep strain was calculated by using DIC as described before. An example set of creep
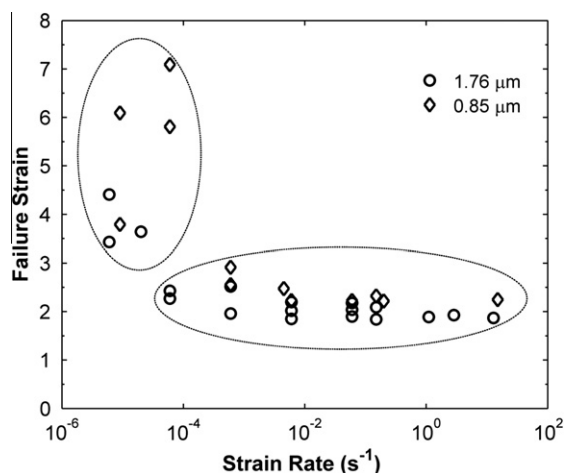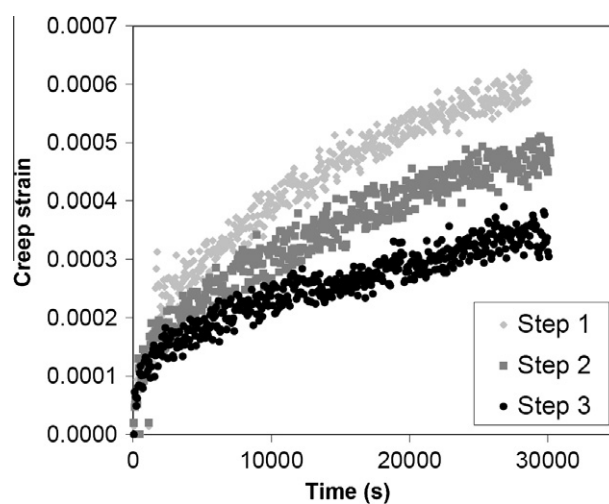

Fig. 8. Strain vs. time of 1.76 μm thick Au films for three cycles at 250 MPa each followed by 3 h at zero stress.

reduction in the activation volume, which are attributed to the significant contribution of grain boundary activity and room temperature primary creep. The steady-state creep rate that is commonly used to investigate grain boundary or dislocation creep was significantly lower ($\leqslant 10^{-8}\,\mathrm{s}^{-1}$), as determined from Fig. 8, and not affected the present experiments because it occurred after a prolonged primary creep phase.

The primary creep rates by themselves are not sufficient to describe the strain evolution under a prescribed load ramp, as shown in Fig. 5. A complete description would require accounting for the entire loading history as the primary creep rate in cyclic creep experiments was found to decrease significantly. Fig. 8 shows the evolution of creep strain (after subtracting the initial elastic strain at $t = 0^+$) at 200 MPa for three successive loading creep cycles. It can be seen that the rate and duration of the primary creep component decreased with the creep cycle. Although all creep curves reached comparable steady-state creep rates, the contribution of the primary creep component was reduced after each cycle. This behavior may be attributed to propagation of initial defects, controlled by the extensive grain boundaries, the primary creep phase. Upon sufficient deformation (time), steady-state nucleation and propagation of defects resulted in steady-state creep at a given applied stress. The experiments in Fig. 5a and b and the creep plots in Fig. 8 point to the important realization that it is not sufficient to measure the inelastic material parameters of nanocrystalline films at the rate of $10^{-4}\,\mathrm{s}^{-1}$, which is commonly done, because for this class of material this rate lies at a pivotal point in the inelastic mechanical behavior.

3.2. Strain rate sensitivity of nanocrystalline Au films

The dependence of inelastic properties of metals on the applied strain rate has been well documented [33]. The yield stress, σ_y, and the strain rate, $\dot{\varepsilon}$, can be related through a power law, $\sigma_y = K\dot{\varepsilon}^m$, where K is a constant and m is the temperature-dependent strain rate sensitivity factor. Ignoring the proportionality constant and taking the logarithm of both sides of the equation, the rate sensitivity factor $m = \log(\sigma_y)/\log(\dot{\varepsilon})$ is calculated. At low temperatures this factor is small, of the order of 0.01 or smaller for microcrystalline fcc metals, while it is as high as 0.1 for body-centered cubic (bcc) metals [33]. However, recent studies reported a variety of rate sensitivity factors for nanocrystalline and ultrafine grain fcc metals, such as Au [13,14], Cu [15] and Ni [5], most of which are of the order of 0.015–0.06 [34]. The increased rate sensitivity of nanocrystalline fcc metals results in hardening and delayed shear localization [2,6,35]. The opposite effect has been observed in nanocrystalline bcc metals, for which the rate sensitivity decreased, despite the increase in yield strength [36]. The associated reduction in the activation volume of fcc metals is due to the small grain size, which promotes grain boundary diffusion and associated plasticity by increasing the net

grain boundary volume and the stresses which drive the grain boundary processes. The significantly increased role of grain boundary processes changes the relative importance of the inelastic deformation mechanisms [35], thus resulting in increased strain rate sensitivity.

Fig. 9a is the log–log plot of the elastic limit and the film yield strength vs. the applied strain rate. The data for the elastic limit and yield strength in Fig. 9a follow bilinear trends (i.e. power laws) and the calculated rate sensitivity factors are indicated next to each fitted line segment. Using the elastic limit, the calculated strain rate sensitivities were 0.03 at strain rates 10^{-4}–20 s^{-1} (for both film thicknesses), and 0.07 and 0.15 for the small and the large thickness, respectively, at strain rates of 10^{-6}–10^{-4} s^{-1}. Strain rate sensitivities between 0.01 and 0.03 have also been reported before for nanocrystalline Ni from tensile and nanoindentation experiments [37] at strain rate regimes corresponding to the fast strain rates applied in the present study. The trends are similar to those obtained using the 0.2% yield
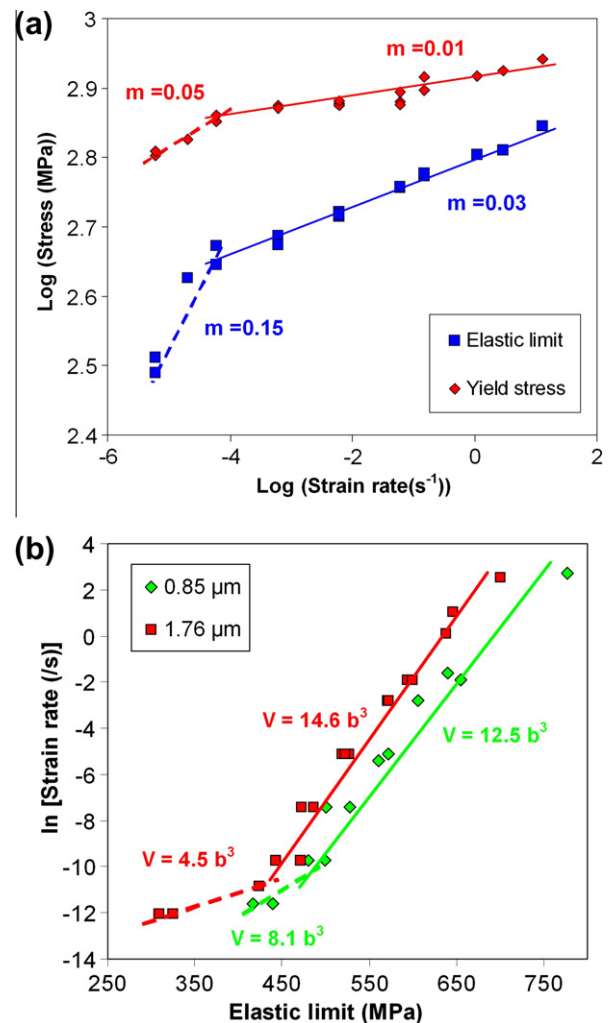

Fig. 9. (a) Rate sensitivity plots for the elastic limit and yield stress for 1.76 μm thick Au specimens. (b) Logarithm of strain rate vs. elastic limit for nanocrystalline Au films with 0.85 and 1.76 μm thickness, with the activation volumes (V) also shown.

strength, but, given that the elastic limit is the first sign of deviation from the elastic behavior, it is considered to be a better parameter with which to assess the contribution of grain boundary processes to the overall inelastic deformation compared to the graphically calculated 0.2% yield strength, which would inevitably include the process of hardening which was not our primary focus.

Fig. 9b is a plot of the natural logarithm of the applied strain rate vs. the elastic limit for the two film thicknesses, from which the activation volume can be calculated as [35]

$$V = \sqrt{3}KT\frac{\delta \ln \dot{\varepsilon}}{\delta \sigma}. \tag{1}$$

Similarly to the strain rate sensitivity factors, the activation volumes also followed bilinear trends. At low strain rates ($\leqslant 10^{-5}\,\text{s}^{-1}$), which are within the rates covered by most literature data for Au films [3,7,14], grain boundary diffusion, grain boundary sliding mediated by dislocation activity and controlled plasticity are the primary reasons for increased rate sensitivity, which is also corroborated by the low activation volumes, i.e. 4.5 and 8.1 b^3. However, even at considerably faster strain rates (10^{-4}–20 s^{-1}), the activation volumes were 12.5 and 14.6 b^3, which are low compared to large-grained Au, and are due to the significant fraction of grain boundaries, which control dislocation nucleation and pinning [8], and to the small grain size, which limits the average dislocation line length. An activation volume of 14 b^3 has also been reported before from tensile experiments on nanocrystalline Ni with 20 nm grain size [37]. The larger activation volumes at rates of 10^{-4}–20 s^{-1} are strong indication of intragranular dislocation based plasticity, as opposed to the slower strain rates when grain boundary processes dominate. Smaller activation volumes, between 2.7 and 5.6 b^3, have been reported from aluminum nanopost compression experiments at a nominal strain rate of 0.02 s^{-1} [38]. The activation volumes from nanopost experiments have been related to dislocation nucleation, while the smaller activation volumes in the current work at lower strain rates represent the combined effect of grain boundary diffusion, grain boundary sliding and dislocation nucleation required to mediate these mechanisms. The low activation volumes reported from nanopost experiments at rates comparable to our fast strain rates are in agreement with experimental observations where the activation volumes calculated from nanoindentation experiments (7 b^3) were half of those calculated from tensile experiments (14 b^3) on the same nanocrystalline Ni [37]. The strain rate sensitivities, m, and the activation volumes, V, for each film thickness, calculated using the elastic limit and the 0.2% yield strength values, are listed in Table 2.

Similar arguments can be made based on the strain rate sensitivity plots. There is a fivefold increase in the strain rate sensitivity factors at $\leqslant 10^{-4}\,\text{s}^{-1}$ for 1.76 μm films, supporting the aforementioned argument for significant contribution of room temperature creep to the inelastic film deformation. The significant contribution of room temper-

ature creep to the mechanics of the present films is possible due to the large elastic stresses that are attainable in the material because of the lack of large defects to initiate localization and, more importantly, the small grain size that supports a strong Hall–Petch effect. Therefore, at the high stresses (450–700 MPa) at which the Au films reached their elastic limit at 10^{-4}–20 s^{-1}, it is expected that intra-granular dislocation plasticity [4,36] dominates, while at the slower strain rates, 10^{-6}–$10^{-4}\,\text{s}^{-1}$, grain boundary diffusion and dislocation nucleation and pinning processes play a major role in inelastic deformation, as supported by the marked change in the rate sensitivity factor at $10^{-4}\,\text{s}^{-1}$.

3.3. Damage evolution as a function of strain rate

Failure at all strain rates and for both film thicknesses occurred by shear localization, as shown in Fig. 10a and 10b, which are the top film surface SEM micrographs of the fracture cross-section of Au specimens loaded at 10^{-6} and $10^{-1}\,\text{s}^{-1}$, respectively. At $10^{-6}\,\text{s}^{-1}$, the failure cross-section was considerably thinner in the wide shear localized region, which supported the large ductilities shown in Fig. 7. The surface and volume voids in the damage zone in Fig. 10a extended as far as 5 μm away from the failure line. On the other hand, the shear bands in Au films loaded at $10^{-1}\,\text{s}^{-1}$ were narrower and had a few surface voids, which were limited to a small region near the failure line, as shown in Fig. 10b. Although the distribution of voids was uniform in the cross-sections of films loaded at 10^{-6} and $10^{-5}\,\text{s}^{-1}$, this was not the case for the specimens loaded at $10^{-1}\,\text{s}^{-1}$ or faster. The fracture surface of these samples was dominated by large film mid-plane voids, as shown in the insert in Fig. 10c, where large voids, formed before shear flow, and catastrophic crack propagation are shown in the same figure. These significant voids were present in both film thicknesses loaded at fast strain rates, while very few microvoids are seen on the specimen top surface in Fig. 10b. In general, at strain rates above $10^{-2}\,\text{s}^{-1}$ failure nucleated at the center of the specimen width, where large microvoids were observed in the film mid-plane. This is the first account of large void formation in the shear localization band of films without the serrated type of failure reported previously [3,19]. Void growth has been reported in the literature in larger scale Ni [4] and Ni–Fe [39] specimens with thicknesses of the order of 100 μm.

In the present experiments, the growth of large mid-plane voids was due to significant triaxial stresses developed at grain boundaries and between the deposition layers of Au seen in Fig. 2c [40]. The high yield strength (~850 MPa) at the fast strain rates and the property mismatch between differently oriented grains caused high local stresses responsible for local slip, hardening and eventually void formation. Contrary to the film surface, the lateral constraints are the strongest inside the film, where the condition of plane stress ceases to apply due to local polycrystalline inhomogeneity, hence large voids can form. At slow strain

Table 2
Strain rate sensitivities, m, and activation volumes, V, for each film thickness, calculated using the elastic limit and the 0.2% yield strength values.

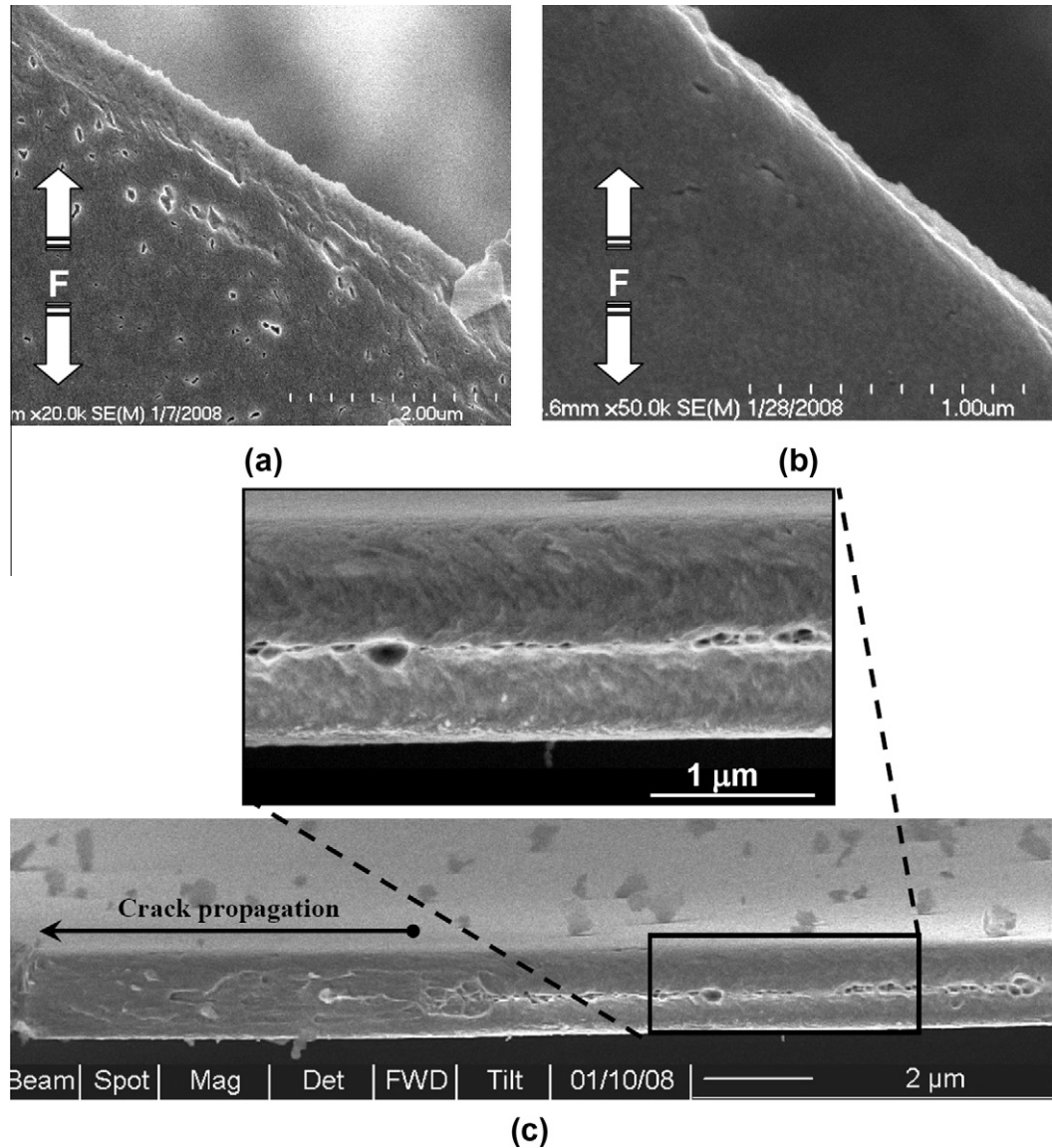| Strain rate (s^{-1})	Film thickness (µm)	$m_{\text{elastic limit}}$	$m_{\text{yield strength}}$	$V_{\text{elastic limit}}$ (b^3)	$V_{\text{yield strength}}$ (b^3)
10^{-6}–10^{-4}	0.85	0.07	0.1	8.1	4
	1.76	0.15	0.05	4.5	8.2
10^{-4}–20	0.85	0.03	0.02	12.5	15.6
	1.76	0.03	0.01	14.6	21.5

Fig. 10. Top surfaces of specimen fracture cross-sections, loaded at (a) 10^{-6} s^{-1} and (b) 10^{-1} s^{-1}. The arrows point to the direction of the applied far-field load. (c) Fracture cross-section of a specimen loaded at 10^{-1} s^{-1}, with the insert showing large void growth before catastrophic crack initiation.

rates the film stress does not reach as high values, while the slow process of loading provides sufficient time for local stress relaxation and more uniform growth and coalescence of small voids that are evenly distributed in the entire film cross-section, which, in turn, leads to wider shear bands and larger ductilities. Once a localized shear band forms across the specimen, the applied strain rate in that region increases as most of the deformation is concentrated in this

small region due to the reduced cross-sectional area. For a rate-sensitive material, the increased deformation rate causes hardening in the localization region, preventing early failure. As a result, the width of the shear localization band increases, as was evident in the slower rate experiments. This is consistent with previous reports on increased rate sensitivity, which stabilizes shear localization and thus delays failure allowing for large strains [41]. Therefore, the strain rate does

affect both void nucleation and growth. Void nucleation in nanocrystalline materials has been investigated by several groups [8,42]. Using atomistic simulations of nanocrystalline metals [8], Van Swygenhoven suggested that shear and hydrostatic stresses develop at grain boundary ledges and triple junctions due to grain sliding incompatibility. Thus, grain boundaries act as sources for emission of dislocations and partials. Similarly, Kumar et al. [4] suggested that, in the early stages of deformation, dislocations are emitted from grain boundaries when intragranular slip is coupled with incompatible grain boundary sliding, which facilitates void formation at the grain boundaries. Grain boundary sliding can lead to voids at triple junctions, unless it is accommodated by diffusion or power law creep, which are insignificant at strain rates faster than $10^{-4}\,s^{-1}$. Thus, this mechanism is responsible for void nucleation at the faster strain rates. Such voids are known to grow in shear [43] to relieve the constraints by a grain or a group of surrounding grains. Since the grains near the center of the specimen are the most constrained, the voids at the mid-film plane will grow and coalesce faster. In contrast, significant creep relaxes the effect of local constraints at the slower strain rates. The large elastic limits measured even at the slow strain rates amplified the local mismatch stresses at grain boundaries which lead to voiding. At slow strain rates, void nucleation can originate in vacancy diffusion and accumulation, along with other creep cavitation processes [44]. Thus, the damage observed at slow rates is well distributed in the film cross-section. It should be noted that in all specimens tested the density and size of pre-existing voids were beyond the imaging resolution of both an SEM and a TEM, as shown in Fig. 2a, c and d. The distinct difference in damage evolution processes at different strain rates emphasizes the need for understanding of the three-dimensional damage evolution in nanocrystalline fcc thin films.

4. Conclusions

The strain rate sensitivity of free-standing nanocrystalline Au films with 40 nm average grain size was experimentally investigated over a wide range of strain rates, 6×10^{-6}–$20\,s^{-1}$, by a custom-built experimental apparatus for microscale films. The experimental apparatus and methods were verified for accuracy through the various strain rates by the consistent elastic moduli of free-standing Au films at all strain rates, averaging 66 ± 4.5 GPa. The free-standing Au films of both thicknesses were strain rate sensitive, were characterized by small activation volumes (4.5 and 8.1 b^3 vs. 12.5 and 14.6 b^3 at strain rates lower and higher than $10^{-4}\,s^{-1}$, respectively) and by very high inelastic property values due to their small grain size. Interestingly, the yield and ultimate tensile strengths approached the same value of ~900 MPa at strain rates faster than $10^{-1}\,s^{-1}$. The very high elastic stresses even at slow loading rates increased the contribution of primary creep, at an initial rate $\geqslant 10^{-7}\,s^{-1}$, which influenced the slow strain rate response and increased the material rate

sensitivity at loading rates slower than $10^{-5}\,s^{-1}$. The two different regimes of strain rate sensitivity established with respect to rates 10^{-5}–$10^{-4}\,s^{-1}$ point to the important realization that knowledge of the inelastic material parameters of nanocrystalline films at the commonly used strain rate of $10^{-4}\,s^{-1}$ is not sufficient because this rate could be a pivotal point in the inelastic mechanical behavior of nanocrystalline films.

Film failure occurred by shear localization at all strain rates, even when the yield strength approached the material tensile strength. However, the extent of void growth decreased and the void size increased with increasing strain rate, while strain hardening and strain rate hardening stabilized shear localization at the lower strain rates. High stress triaxiality in the film mid-plane and fast loading rates resulted in constrained void growth in the film mid-plane. These large voids resulted in smaller strain at catastrophic crack initiation and small shear localization zones, compared to an abrupt increase in the size of the shear localization zone at strain rates lower than $\leqslant 10^{-4}\,s^{-1}$, which was supported by small distributed voids. From the two modes of failure reported here, it is concluded that even for a very large number of grains across the thickness of nanocrystalline films, which establishes a statistically homogeneous film, damage initiates and progresses in a three-dimensional manner and may not be appropriately described by a two-dimensional analysis.

References

[1] Artz E. Acta Mater 1998;46:5611.
[2] Meyers MA, Mishra A, Benson DJ. Prog Mater Sci 2006;51:427.
[3] Chasiotis I, Bateson C, Timpano K, McCarty A, Barker NS, Stanec J. Thin Solid Films 2006;515:3183.
[4] Kumar KS, Suresh S, Chisholm MF, Horton JA, Wang P. Acta Mater 2003;51:387.
[5] Schwaiger R, Moser B, Dao M, Chollacoop N, Suresh S. Acta Mater 2003;51:5159.
[6] Kumar KS, Van Swygenhoven H, Suresh S. Acta Mater 2003;51:5743.
[7] Wang L, Prorok BC. J Mater Res 2008;23:55.
[8] Van Swygenhoven H. Mater Sci Eng A 2008;483:33.
[9] Wei Y, Bower AF, Gao H. J Mech Phys Solids 2008;56:1460.
[10] Coble RL. J Appl Phys 1962;34:1679.
[11] Shan Z, Stach EA, Wiezorek JMK, Knapp JA, Follstaedt DM, Mao SX. Science 2004;305:654.
[12] Langdon TG. J Mater Sci 2006;41:597.
[13] Emery RD, Povirk GL. Acta Mater 2002;51:2067.

[14] Emery RD, Povirk GL. Acta Mater 2002;51:2079.

[15] Jiang Z, Liu X, Li G, Jiang Q, Lian J. Appl Phys Lett 2006;88:43115.

[16] Hyun S, Brown WL, Vinci RP. Appl Phys Lett 2003;83:4411.

[17] Wang N, Wang Z, Aust KT, Erb U. Mater Sci Eng A 1997;237:150.

[18] Sanders PG, Rittner M, Kiedaisch E, Weertman JA, Kung H, Lu YC. Nanostruct Mater 1997;9:433.

[19] Espinosa HD, Prorok BC, Peng B. J Mech Phys Solids 2004;52:667.

[20] Chauhan S, Bastawros AF. Appl Phys Lett 2008;93:041901.

[21] Jonnalagadda K, Chasiotis I, Yagnamurthy S, Lambros J, Polcawich R, Pulskamp J, et al. Exp Mech 2010;50:25.

[22] Callister Jr WD. Materials science and engineering. New York: Wiley; 1994.

[23] Lapman S. ASM handbook, vol. 2. ASM International; 1990. p. 704.

[24] Haque MA, Saif MTA. Proc Natl Acad Sci 2004;101:6335.

[25] Long GS, Read DT, MsColskey JD, Crago K. ASTM STP 2001;1413:262.

[26] Sanders PG, Eastman JA, Weertman JR. Acta Mater 1997;45:4019.

[27] Hugo RC, Kung H, Weertman JR, Mitra R, Knapp JA, Follstaedt DM. Acta Mater 2003;51:1937.

[28] Korn D, Morsch A, Birringer R, Arnold W, Gleiter H. J Phys C 1998;5:769.

[29] Kalkman AJ, Verbruggen AH, Janssen GC. Appl Phys Lett 2001;78:2673.

[30] Yan X, Brown WL, Li Y, Papapolymerou J, Palego C, Hwang JCM, et al. J MEMS 2009;18:570.

[31] Vinci RP, Cornella G, Bravman JC. In: Proceedings of the 5th international workshop on stress induced phenomena in metallization, Stuttgart; 1999. p. 240.

[32] Baker SP, Vinci RP, Arias T. MRS Bull 2002;27:26.

[33] Hertzberg RW. Deformation and fracture mechanics of engineering materials. New York: John Wiley & Sons; 1976.

[34] Choi I, Schwaiger R, Kurmanaeva L, Kraft O. Scripta Mater 2009;61:64.

[35] Wei Q. J Mater Sci 2007;42:1709.

[36] Wei Q, Cheng S, Ramesh KT, Ma E. Mater Sci Eng A 2004;381:71.

[37] Gu CD, Lian JS, Jiang Q, Zheng WT. J Phys D Appl Phys 2007;40:7440.

[38] Mook WM, Lund MS, Leighton C, Gerberich WW. Mater Sci Eng A 2008;493:12.

[39] Ebrahimi F, Ahmed Z, Li HQ. Mater Manuf Processes 2006;21:687.

[40] Fleck NA, Hutchinson JW. Proc Roy Soc London A 1986;407:435.

[41] Ghosh AK. Acta Metall 1977;25:1413.

[42] Dongare AM, Rajendran AM, LaMattina B, Zikry MA, Brenner DW. Phys Rev B 2009;80:104108.

[43] Meyers MA, Traiviratana S, Lubarda VA, Benson DJ, Bringa EM. J Mater 2009;61:35.

[44] Balluffi RW, Seigle LL. Acta Metall 1957;5:449.